
A World Model of Radiologist Reading for Medical Image Representation Learning

Yiwei Li* **Zihao Wu*** **Huaqin Zhao** **Yifan Zhou**
University of Georgia University of Georgia University of Georgia University of Georgia

Chao Cao **Dajiang Zhu** **Tianming Liu**
University of Texas at Arlington University of Texas at Arlington University of Georgia

Lin Zhao[†]
New Jersey Institute of Technology

Abstract

Radiologist eye-tracking data provide a rich record of how experts search, compare, and accumulate evidence during image reading; yet, existing methods exploit this signal only partially, either as a static spatial prior or as an auxiliary prediction target decoupled from diagnosis. We propose GazeWorld, a medical imaging world model that treats the image as the world and the radiologist’s fixation sequence as a trajectory through it. GazeWorld autoregressively predicts the latent representation of the next fixated patch from all previously visited ones, while a spatial-completion branch covers unvisited regions. At inference, GazeWorld generates a sequence of patch representations from the image alone without requiring real gaze data. Frozen GazeWorld features achieve state-of-the-art diagnostic accuracy across all nine supervised settings on CheXpert, RSNA Pneumonia, and SIIM-ACR Pneumothorax, as well as the highest zero-shot accuracy on all three benchmarks. On the GazeSearch benchmark, a generic decoder trained on the same frozen features outperforms the purpose-built LogitGaze-Med by over 16% in ScanMatch and 22% in SED, despite not being explicitly trained to predict gaze. GazeWorld demonstrates that modeling how experts read, not just what they conclude, offers a promising pretraining paradigm for medical imaging AI.

1 Introduction

Two dark clouds loom over the clinical translation of medical imaging AI. Large-scale medical imaging datasets remain scarce because acquisition is bound by clinical access, cross-institutional sharing is curtailed by privacy regulations, and expert annotations are prohibitively expensive to obtain at scale [Irvin et al., 2019, Johnson et al., 2019, Rajpurkar et al., 2017]. Without sufficiently large and diverse training sets, models readily overfit to dataset-specific shortcuts and degrade under distribution shifts [Azizi et al., 2021, Sowrirajan et al., 2021]. Compounding this data bottleneck, most current models emit a diagnostic label without exposing the evidence behind the prediction [Chen et al., 2024, Zhou et al., 2023], leaving clinicians unable to assess whether the output reflects sound reasoning or a spurious shortcut and ultimately eroding trust required for clinical deployment.

Radiologist gaze offers a promising inroad into both challenges. Eye-tracking data encode expert prior knowledge about where diagnostically relevant evidence lies, providing a form of supervision

*Equal contribution.

[†]Corresponding author.

that can reduce reliance on large labeled datasets; several studies have incorporated gaze as a spatial attention prior and demonstrated improved performance [Shentu and Al Moubayed, 2024, Wang et al., 2022a, Ma et al., 2024, Wang et al., 2025], though collapsing eye movements into static heatmaps discards the order in which evidence was gathered. Beyond this, gaze trajectories record the temporal sequence in which a radiologist searches, compares, and accumulates evidence, offering an observable trace of diagnostic reasoning that can guide models toward interpretable decisions. Recent work has shown that such trajectories can be predicted from chest radiographs alone [Pham et al., 2025, Lvov and Pershin, 2025], but the predicted scanpaths remain decoupled from the diagnosis. Both lines leave the temporal structure of radiologist evidence gathering unused for diagnosis.

We propose to close this gap by formulating a world model of the radiologist’s diagnostic process. When reading a medical image, a radiologist navigates a perceptual world defined by the image. At each fixation, the radiologist extracts local evidence and selects the next region of interest conditioned on prior observations, iterating until sufficient evidence supports a diagnosis. We formalize this as a world model that predicts the latent representation of each successive fixation, conditioned on the current fixation and accumulated evidence. Each fixation along the trajectory thus becomes a prediction target, yielding dense self-supervised signals from each image without requiring diagnostic labels. At the same time, the learned representation retains the sequential structure of expert reasoning, offering a basis for interpretability that static attention maps cannot provide.

We instantiate this formulation as GazeWorld, a medical imaging world model that captures the sequential structure of expert reading through gaze-ordered representation prediction. A visual encoder maps the image into patch-level representations and an autoregressive predictor, following the joint-embedding predictive architecture (JEPA) [LeCun et al., 2022, Assran et al., 2023], processes the gaze-ordered fixation sequence to predict the latent representation of the next fixated patch from all previously visited ones. In parallel, a spatial-completion branch uses the full gaze context to predict the representations of all unvisited patches. At inference, the autoregressive predictor generates the representations from the image alone without requiring gaze data for downstream tasks.

We evaluate GazeWorld on chest radiograph diagnosis and scanpath prediction. For diagnosis, linear probes on frozen GazeWorld features achieve state-of-the-art accuracy across all nine supervised settings on CheXpert [Irvin et al., 2019], RSNA Pneumonia [Colak et al., 2021], and SIIM-ACR Pneumothorax [Zawacki et al., 2019], as well as the highest zero-shot accuracy on all three benchmarks. For scanpath prediction, a generic decoder trained on the same frozen features outperforms the purpose-built LogitGaze-Med [Lvov and Pershin, 2025] by over 16% in ScanMatch and 22% in SED on the GazeSearch benchmark, despite not being explicitly trained to predict gaze.

Our contributions are as follows:

- We introduce the concept of a gaze world model for medical imaging, which formulates the radiologist’s reading process as a trajectory through a perceptual world defined by the image. This formulation fully exploits the temporal structure of expert gaze as a self-supervised training signal, moving beyond static heatmaps and decoupled scanpath prediction.
- We instantiate this formulation as GazeWorld, which combines gaze-ordered autoregressive prediction in latent space with a spatial-completion branch for unvisited regions, shaping the representation to capture both diagnostic content and sequential reading structure.
- GazeWorld achieves state-of-the-art diagnostic accuracy across all nine supervised settings and the highest zero-shot accuracy on three chest radiograph benchmarks. A generic decoder on the same frozen features outperforms purpose-built scanpath predictors, showing that a single representation supports both accurate diagnosis and interpretable scanpath decoding.

2 Related Work

2.1 Gaze Supervision and Scanpath Prediction

Radiologist gaze has been used in medical AI mainly in two ways. The first uses gaze as spatial supervision for diagnosis or representation learning, typically by converting fixations into heatmaps, attention maps, or relation matrices [Wang et al., 2022a, Saab et al., 2021, Stember et al., 2019, Hsieh et al., 2024]. These signals provide weak but clinically meaningful localization cues, helping models attend to regions that radiologists consider diagnostically relevant. For example, EGMA [Ma

et al., 2024] uses fixation-derived attention to guide fine-grained image-text alignment, while eCLIP [Kumar and Marttinen, 2024] and other gaze-guided methods use expert attention to regularize contrastive learning, region-aware prediction, or diagnostic reasoning. These approaches demonstrate that gaze can improve clinical relevance and reduce reliance on dense manual annotations. However, they mostly treat gaze as static spatial supervision, preserving where radiologists looked while discarding the temporal order of evidence gathering, comparison, and integration.

The second line models gaze as a scanpath prediction problem. GazeFormer [Mondal et al., 2023], HAT [Yang et al., 2024], MedGaze [Awasthi et al., 2025], GazeSearch [Pham et al., 2025], and LogitGaze-Med [Lvov and Pershin, 2025] predict fixation trajectories or dwell times from medical images. These methods explicitly preserve gaze order and evaluate human-like visual search, but scanpath prediction is usually treated as a standalone output task. In contrast, GazeWorld uses radiologist scanpaths to define the autoregressive prediction order for representation learning, so the temporal structure of expert search directly shapes the visual encoder.

2.2 World Models and Representation-Space Prediction

World models aim to learn predictive structure in latent space as observations accumulate [LeCun et al., 2022]. Instead of reconstructing pixels, JEPA-style methods predict abstract representations of unseen regions from visible context, which makes the objective less sensitive to low-level appearance noise and more focused on semantic structure [Assran et al., 2023, Bardes et al., 2023]. Autoregressive vision models provide another predictive formulation by modeling visual tokens sequentially, but their prediction order is usually fixed by design, such as raster scan or predefined token layouts [Chen et al., 2020, El-Nouby et al., 2024]. These predictive objectives are especially appealing for medical imaging, where diagnostic signals are subtle, spatially distributed, and often better captured in representation space than at the pixel level. Recent medical models such as CheXWorld [Yue et al., 2025] and US-JEPA [Radhachandran et al., 2026] show that representation-space prediction can improve medical visual features by modeling anatomy, global layout, and domain variation.

However, existing predictive structures are typically defined by random masks, block masks, crops, or raster order. These choices are convenient but not tied to clinical reading behavior. GazeWorld instead uses radiologist fixation sequences as the prediction structure, where previously fixated patches form the context and the next expert-fixated patch is the autoregressive target. This grounds representation-space prediction in the temporal process of diagnostic evidence accumulation.

2.3 Medical Vision Representation Learning

Medical vision models rely on supervised pretraining, self-supervised learning, contrastive learning, and vision-language pretraining to reduce annotation cost and improve transfer [Irvin et al., 2019, Johnson et al., 2019, Rajpurkar et al., 2017, Sowrirajan et al., 2021, Azizi et al., 2021, Xiao et al., 2023]. Representative medical vision-language models include GLoRIA [Huang et al., 2021], MedCLIP [Wang et al., 2022b], BioViL [Bannur et al., 2023], MGCA [Wang et al., 2022c], MedKLIP [Wu et al., 2023], and PRIOR [Cheng et al., 2023], which learn transferable representations from image labels, unlabeled images, or image-text pairs.

GazeWorld is complementary to these pretraining paradigms rather than a replacement for them. It can be applied on top of existing medical visual backbones, such as MGCA, EGMA, or MedCLIP, to further refine their representations with expert gaze dynamics. Thus, our contribution is not a new foundation pretraining pipeline from scratch, but a gaze-ordered world-model refinement objective that injects radiologist reading behavior into already pretrained medical encoders.

3 Method

GazeWorld casts the medical image as a perceptual world and the radiologist’s fixation sequence as a trajectory through it. An autoregressive predictor processes the gaze-ordered fixation sequence and predicts the latent representation of the next fixated patch from all previously visited ones, turning each fixation into a self-supervised training signal. To exploit unvisited regions, a spatial-completion branch uses the full gaze context to predict all unvisited patch representations in parallel. The final pretraining objective combines next-fixation prediction with gaze-conditioned spatial completion.

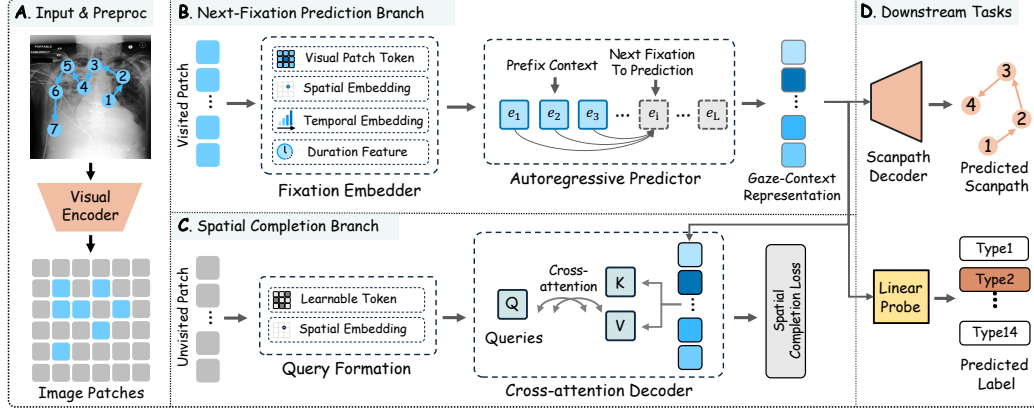


Figure 1: **GazeWorld overview.** After the chest radiograph and radiologist fixation sequence are processed in Part A, the image is converted into patch-level semantic tokens and the patch grid is divided into visited and unvisited regions. In Part B, visited patch tokens are combined with spatial, temporal, and duration information by the fixation embedder, and an autoregressive predictor performs latent-space prediction of the next expert-fixated representation from the prefix context. The resulting gaze-context representation is then used in Part C, where unvisited patch queries are formed from learnable tokens and spatial embeddings and completed through a cross-attention decoder. Finally, Part D evaluates the representations via scanpath decoding and diagnostic linear probing.

3.1 Patch Representations and Fixation Sequence

Following the input and preprocessing stage in Fig. 1A, let \mathbf{X} denote a medical image. An online visual encoder ϕ maps \mathbf{X} into a set of patch-level semantic representations:

$$\mathbf{Z} = \phi(\mathbf{X}) = \{\mathbf{z}_p\}_{p=1}^N, \quad \mathbf{z}_p \in \mathbb{R}^d, \quad (1)$$

where \mathbf{Z} denotes the set of all patch-level representations, \mathbf{z}_p is the d -dimensional semantic representation of the p -th image patch, and N is the number of image patches. The visual encoder is initialized from a pretrained model and adapted by the gaze-ordered objective.

Each image is paired with a fixation sequence $\mathcal{F} = \{f_1, \dots, f_T\}$, where $f_t = (x_t, y_t)$ denotes the coordinates of the t -th fixation. We assign each fixation to its nearest image patch and merge repeated visits to the same patch while preserving the first-visit order. This yields an ordered sequence of unique visited patch indices, denoted by \mathcal{S} :

$$\mathcal{S} = (s_1, \dots, s_L), \quad s_i \in \{1, \dots, N\}. \quad (2)$$

3.2 Next-Fixation Prediction

As illustrated in Fig. 1B, the next-fixation branch uses an autoregressive predictor to forecast the latent representation of each successive expert-fixated region from all preceding fixations. For each visited patch s_i in \mathcal{S} , we construct a fixation token by combining its visual representation with positional and temporal cues:

$$\mathbf{h}_i = \psi(\mathbf{z}_{s_i}, \mathbf{e}_{s_i}, i, \Delta_i), \quad (3)$$

where \mathbf{e}_{s_i} is the spatial embedding of patch s_i , i the temporal rank of the fixation, Δ_i its dwell duration, and ψ the fixation embedder. Following the JEPa [LeCun et al., 2022, Assran et al., 2023], which learns by predicting target representations rather than reconstructing raw inputs, an autoregressive predictor g_θ with a causal attention mask receives the prefix of visited fixation tokens and predicts the representation of the next fixated patch:

$$\hat{\mathbf{z}}_{s_i} = g_\theta(\mathbf{h}_1, \dots, \mathbf{h}_{i-1}), \quad i = 2, \dots, L. \quad (4)$$

Prediction targets come from a momentum target encoder $\bar{\phi}$, an exponential-moving-average (EMA) copy of the online visual encoder ϕ [Grill et al., 2020]. While ϕ is directly optimized by gradient

descent, $\bar{\phi}$ is updated via stop-gradient after each optimization step, providing a stable representation space for the prediction objective:

$$\bar{\mathbf{z}}_{s_i} = \bar{\phi}(\mathbf{X})_{s_i}, \quad (5)$$

$$\bar{\theta}_\phi \leftarrow \tau \bar{\theta}_\phi + (1 - \tau)\theta_\phi, \quad (6)$$

where θ_ϕ and $\bar{\theta}_\phi$ denote the parameters of the online visual encoder and the target encoder, respectively. The autoregressive loss is

$$\mathcal{L}_{\text{AR}} = \frac{1}{L-1} \sum_{i=2}^L \text{SmoothL1}(\text{LN}(\hat{\mathbf{z}}_{s_i}), \text{sg}(\bar{\mathbf{z}}_{s_i})), \quad (7)$$

where $\text{LN}(\cdot)$ denotes layer normalization and $\text{sg}(\cdot)$ stop-gradient. Following the JEPA principle, prediction operates in representation space rather than pixel space, encouraging the model to capture anatomical and diagnostic regularities that make expert fixation order predictable.

3.3 Spatial Completion

As shown in Fig. 1C, the spatial-completion branch complements the autoregressive objective, which supervises only the patches that appear in the radiologist’s fixation sequence. However, unvisited regions can still be clinically informative. For example, a region may be skipped because it is normal, because it is peripheral to the suspected finding, or because the accumulated context is already sufficient. We therefore introduce a spatial-completion branch that assigns a representation-space target to every unvisited patch.

Let

$$\mathcal{U} = \{1, \dots, N\} \setminus \{s_1, \dots, s_L\} \quad (8)$$

denote the set of unvisited patches. A lightweight cross-attention decoder d_ξ predicts one representation for each unvisited patch. Queries combine a learnable mask token with the spatial embedding of the target patch; keys and values come from the gaze-context representation:

$$\hat{\mathbf{r}}_p = d_\xi(\mathbf{m}_p + \mathbf{e}_p, \mathbf{H}), \quad p \in \mathcal{U}, \quad (9)$$

where

$$\mathbf{H} = g_\theta(\mathbf{h}_1, \dots, \mathbf{h}_L) \quad (10)$$

is the full fixation-context representation produced by the autoregressive predictor. The spatial-completion loss matches each prediction to the corresponding momentum target:

$$\mathcal{L}_{\text{SC}} = \frac{1}{|\mathcal{U}|} \sum_{p \in \mathcal{U}} \text{SmoothL1}(\text{LN}(\hat{\mathbf{r}}_p), \text{sg}(\text{LN}(\bar{\mathbf{z}}_p))). \quad (11)$$

This objective resembles masked representation prediction [Assran et al., 2023], but derives its context from the radiologist’s reading trajectory rather than random visible patches. The model thus learns to infer unvisited anatomy from the evidence that an expert chose to inspect.

3.4 Pretraining Objective

The complete world-model pretraining objective combines autoregressive next-fixation prediction and spatial completion:

$$\mathcal{L}_{\text{pre}} = \mathcal{L}_{\text{AR}} + \lambda \mathcal{L}_{\text{SC}}. \quad (12)$$

During pretraining, the online visual encoder is optimized jointly with the fixation embedder, autoregressive predictor, prediction head, and spatial-completion decoder. The target encoder receives no gradients and is updated only through EMA (6).

4 Experiments

4.1 Experimental Setup

We evaluate GazeWorld on diagnostic classification and scanpath prediction.

Table 1: Comparison of supervised classification AUROC on CheXpert [Irvin et al., 2019], RSNA [Colak et al., 2021], and SIIM-ACR [Zawacki et al., 2019] with 1%, 10%, and 100% of training labels. **Best** and second-best results are highlighted.

Method	CheXpert			RSNA			SIIM-ACR		
	1%	10%	100%	1%	10%	100%	1%	10%	100%
BioViL [Bannur et al., 2023]	54.19	60.37	66.55	70.74	72.84	78.48	62.98	68.39	78.20
MedKLIP [Wu et al., 2023]	-	-	-	79.43	78.62	82.76	74.50	78.27	84.67
MGCA [Wang et al., 2022c]	67.12	76.10	81.57	80.41	85.67	88.24	86.14	<u>88.13</u>	<u>91.84</u>
GLoRIA [Huang et al., 2021]	67.40	77.37	81.74	81.90	81.24	88.57	-	-	-
PRIOR [Cheng et al., 2023]	65.51	70.70	79.11	79.74	79.72	83.95	81.96	82.76	85.33
CheXWorld [Yue et al., 2025]	62.81	80.03	85.39	78.30	84.12	<u>88.66</u>	62.31	81.54	91.34
MedCLIP [Wang et al., 2022b]	<u>74.65</u>	<u>82.88</u>	<u>85.58</u>	82.31	84.16	87.86	86.09	87.41	91.46
EGMA [Ma et al., 2024]	71.21	79.79	85.45	<u>82.49</u>	<u>84.73</u>	88.09	<u>87.17</u>	87.91	88.98
Ours	78.37	83.41	87.61	83.27	85.75	90.15	87.85	90.48	94.27

Diagnostic classification. We evaluate frozen backbone features of GazeWorld on CheXpert [Irvin et al., 2019], RSNA Pneumonia [Colak et al., 2021], and SIIM-ACR Pneumothorax [Zawacki et al., 2019] under 1%, 10%, and 100% label fractions, as well as zero-shot transfer on all three benchmarks. We compare against BioViL [Bannur et al., 2023], MedKLIP [Wu et al., 2023], MGCA [Wang et al., 2022c], GLoRIA [Huang et al., 2021], PRIOR [Cheng et al., 2023], MedCLIP [Wang et al., 2022b], CheXWorld [Yue et al., 2025], and EGMA [Ma et al., 2024].

Scanpath prediction. We pretrain on MIMIC-EYE [Hsieh et al., 2023] and probe on GazeSearch [Pham et al., 2025], a refined scanpath benchmark derived from MIMIC-EYE with more precise gaze-path annotations, under the ChestSearch protocol. For each backbone variant, we freeze the pretrained visual encoder and train only the same lightweight scanpath decoder on top of its patch-level features; performance differences therefore reflect scanpath-relevant information already encoded in the frozen representations. We compare against representative scanpath prediction methods, including general visual-search baselines GazeFormer [Mondal et al., 2023] and HAT [Yang et al., 2024], radiology-specific GazeSearch [Pham et al., 2025], and the recent LogitGaze / LogitGaze-Med models [Lvov and Pershin, 2025], with LogitGaze-Med serving as the strongest scanpath baseline.

All dataset statistics, baseline protocols, and split details are provided in Appendices A.1 and A.2.

4.2 Implementation Details

We use MedCLIP-Swin [Liu et al., 2021] as the visual encoder, processing chest radiographs at 224×224 resolution. The autoregressive predictor is an 8-layer causal Transformer with hidden dimension 768. GazeWorld is pretrained on MIMIC-EYE [Hsieh et al., 2023] for 15 epochs using AdamW [Loshchilov and Hutter, 2017] with learning rate 3×10^{-4} . The spatial-completion weight is set to $\lambda = 1.0$. At evaluation, the visual encoder and predictor are frozen; downstream tasks use only the resulting representations with no access to gaze data. Full architecture specifications, hyperparameters, and evaluation protocols are provided in Appendix B.

4.3 Downstream Classification

If the world model has captured the invariants of expert reading, its representations should also transfer to standard diagnostic tasks. We evaluate frozen backbone features for supervised and zero-shot classification on three external datasets that are not used during world-model pretraining.

Classification results. Tables 1 and 2 summarize supervised and zero-shot diagnostic transfer. In supervised classification, GazeWorld achieves the best AUROC in all nine dataset-label settings. Under the controlled comparison with EGMA, where the Swin backbone, MedCLIP initialization, gaze data, and downstream protocol are matched, GazeWorld improves CheXpert 1% AUROC from 71.21 to 78.37. It also outperforms CheXWorld [Yue et al., 2025] in all settings, with the largest gains in low-label regimes. In zero-shot evaluation, GazeWorld obtains the highest accuracy on all

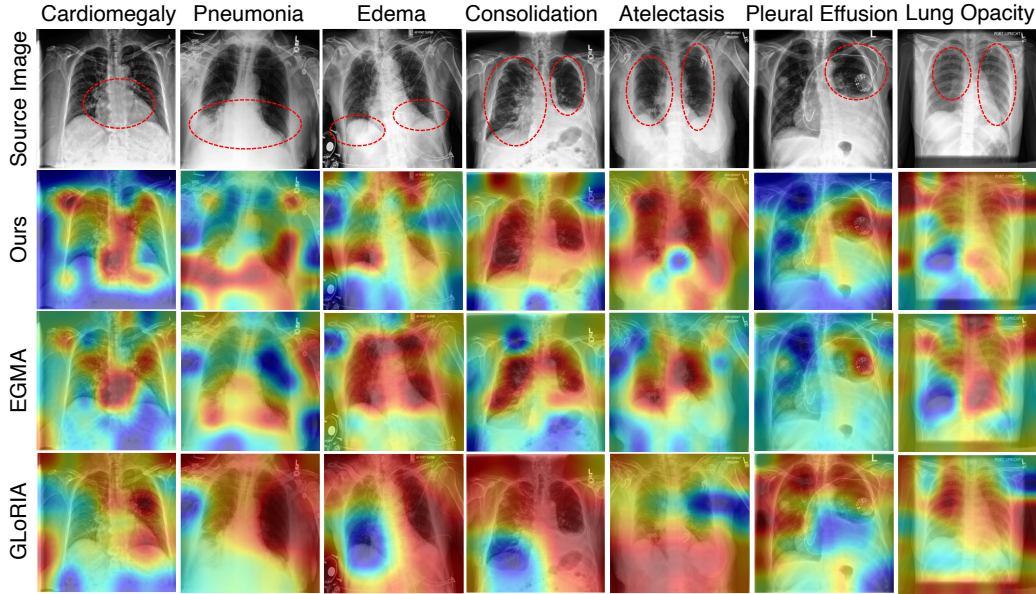


Figure 2: Grad-CAM [Selvaraju et al., 2017] attention visualizations across seven pathologies, comparing the source radiograph, GazeWorld, EGMA [Ma et al., 2024], and GLoRIA [Huang et al., 2021]. **Red dashed circles** on the source radiographs highlight pathology-relevant regions used for visual reference. All maps are generated with the same Grad-CAM protocol (Appendix C).

Table 2: Zero-shot classification on CheXpert 5×200 [Irvin et al., 2019], RSNA [Colak et al., 2021], and SIIM-ACR [Zawacki et al., 2019]. AUROC, Accuracy, and F1 are computed without task-specific fine-tuning. **Best** and second-best results are highlighted.

Method	CheXpert 5×200		RSNA		SIIM-ACR	
	AUROC↑	Acc.↑ / F1↑	AUROC↑	Acc.↑ / F1↑	AUROC↑	Acc.↑ / F1↑
CLIP [Radford et al., 2021]	15.50	19.60 / 10.99	21.67	23.46 / 19.87	42.13	46.11 / 40.13
GLoRIA [Huang et al., 2021]	49.18	51.10 / 47.25	<u>60.77</u>	61.53 / 60.09	–	- / -
MGCA [Wang et al., 2022c]	42.53	43.39 / 39.67	59.19	60.82 / <u>59.57</u>	36.60	38.45 / 34.95
MedCLIP [Wang et al., 2022b]	<u>56.63</u>	<u>57.40 / 55.72</u>	58.08	62.17 / 40.06	56.17	56.89 / 55.44
EGMA [Ma et al., 2024]	56.09	57.15 / 55.03	57.46	66.85 / 43.08	<u>59.79</u>	<u>63.24 / 61.04</u>
Ours	58.13	59.42 / 56.85	62.84	70.18 / 47.31	64.29	66.59 / 63.26

three datasets and the highest F1 on CheXpert and SIIM-ACR. Figure 2 provides qualitative Grad-CAM visualizations under the EGMA protocol (Appendix C), showing that GazeWorld produces more concentrated activations over clinically relevant anatomy than EGMA and GLoRIA. These visualizations are qualitative and are not intended as formal localization evaluations. Training and evaluation details are summarized in Appendix B.

4.4 Scanpath Prediction

A central claim of this work is that world-model pretraining on fixation sequences produces representations that encode the sequential structure of expert reading. We test this claim with a controlled probing experiment. For each backbone variant, we freeze the pretrained visual encoder and train only a lightweight scanpath decoder on top of its patch-level features (Appendix D). The decoder architecture, optimization settings, and training data are kept identical across variants; the only variable is the frozen representation. Thus, performance differences reflect how much scanpath-relevant information is already encoded in the learned features.

Table 3 shows that all three variants of GazeWorld outperform the previous state-of-the-art LogitGazeMed on the main scanpath metrics. The best variant improves ScanMatch [Cristino et al., 2010] by

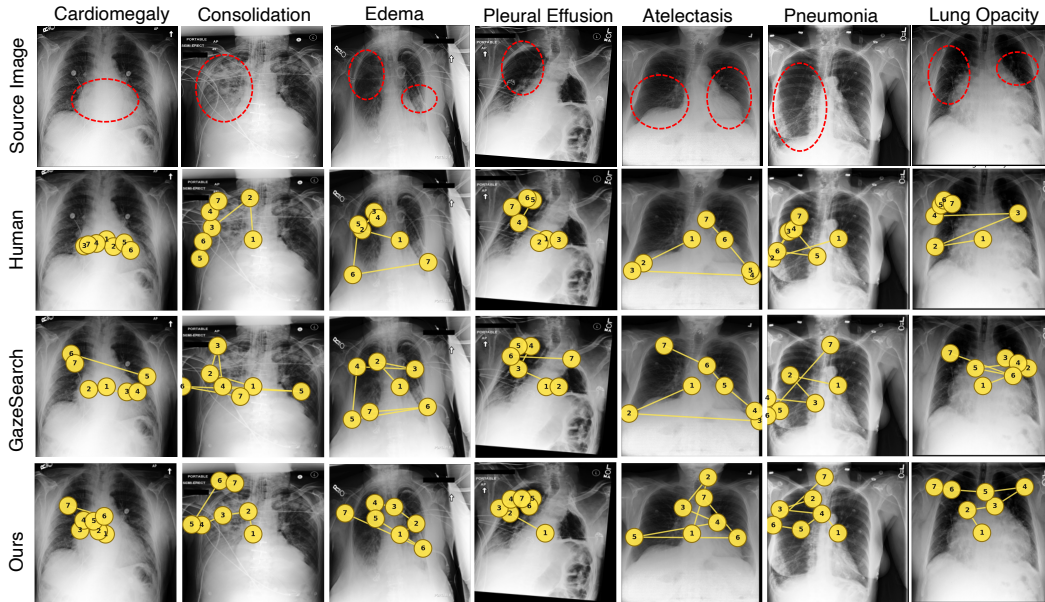


Figure 3: Qualitative scanpath comparison across seven pathologies. The first row shows the source radiographs, with **red dashed circles** marking pathology-relevant regions. We compare human scanpaths, GazeSearch predictions [Pham et al., 2025], and trajectories decoded from frozen GazeWorld representations using the same supervised decoder.

Table 3: GazeSearch scanpath probing results. ScanMatch, STDE, and MultiMatch scores are higher-better, while SED is lower-better. **Best** and second-best results are highlighted.

Method	Scanpath			MultiMatch		
	SM \uparrow	SED \downarrow	STDE \uparrow	Vec. \uparrow	Dir. \uparrow	Pos. \uparrow
GazeFormer [Mondal et al., 2023]	0.280	5.11	0.801	0.902	0.644	0.803
HAT [Yang et al., 2024]	0.296	5.07	0.800	0.909	0.649	0.825
GazeSearch [Pham et al., 2025]	0.351	4.89	0.809	0.917	0.679	0.829
LogitGaze [Lvov and Pershin, 2025]	0.328	5.07	0.810	0.882	0.643	0.809
LogitGaze-Med (Res) [Lvov and Pershin, 2025]	0.416	4.68	0.852	0.935	0.650	0.823
LogitGaze-Med (CheX) [Lvov and Pershin, 2025]	0.419	4.68	0.855	0.938	0.651	0.823
Ours (MedCLIP)	0.479	3.74	0.909	0.941	0.649	0.837
Ours (Res)	<u>0.484</u>	<u>3.66</u>	0.912	<u>0.966</u>	<u>0.678</u>	0.917
Ours (CheX)	0.489	3.63	<u>0.911</u>	0.966	0.686	<u>0.915</u>

over 16%, reduces SED [Foulsham and Underwood, 2008] by more than 22%, and raises STDE [Wang et al., 2011] by over 6% relative to LogitGaze-Med (CheX). Since LogitGaze-Med is a purpose-built scanpath predictor with explicit gaze supervision, whereas our probing uses the same generic decoder on frozen features, these gains suggest that gaze-ordered world-model pretraining encodes scanpath-relevant structure into the learned representation. The same table further reports MultiMatch [Jarodzka et al., 2010] results, with consistent gains across vector, direction, and position.

Figure 3 provides qualitative support for the probing results. Across seven pathologies, scanpaths decoded from GazeWorld features more closely follow radiologist reading trajectories and attend to pathology-relevant anatomy, whereas GazeSearch produces more diffuse fixation sequences.

Table 4: Ablation on fixation ordering, backbone initialization, and objective components. “AR only” denotes next-fixation prediction without spatial completion, and “SC only” denotes spatial completion without autoregressive prediction. All metrics are **zero-shot**: AUROC, Accuracy, and F1 are computed without task-specific fine-tuning.

Variant	CheXpert 5×200		RSNA		SIIM-ACR	
	AUROC↑	Acc.↑ / F1↑	AUROC↑	Acc.↑ / F1↑	AUROC↑	Acc.↑ / F1↑
Raster-scan Order	52.18	55.21 / 51.58	50.39	62.46 / 42.30	53.50	56.22 / 50.16
Random Order	52.25	56.08 / 49.13	51.58	61.53 / 42.68	55.06	57.02 / 54.34
AR Only	57.78	58.86 / 55.91	59.11	68.07 / 44.15	62.10	64.88 / 61.94
SC Only	54.67	54.41 / 53.06	51.25	60.63 / 40.03	52.59	53.72 / 51.37
Ours	58.13	59.42 / 56.85	62.84	70.18 / 47.31	64.29	66.59 / 63.26

Table 5: Effect of backbone initialization on zero-shot classification. AUROC, Accuracy, and F1 are reported on three external datasets.

Backbone	CheXpert 5×200			RSNA			SIIM-ACR		
	AUROC↑	Acc.↑	F1↑	AUROC↑	Acc.↑	F1↑	AUROC↑	Acc.↑	F1↑
MGCA	42.53	43.39	39.67	59.19	60.82	59.57	36.60	38.45	34.95
+GazeWorld	47.41	48.31	46.07	60.76	61.46	59.98	41.07	43.56	39.62
Δ	+4.88	+4.92	+6.40	+1.57	+0.64	+0.41	+4.47	+5.11	+4.67
EGMA	56.09	57.15	55.03	57.46	66.85	43.08	59.77	63.24	61.04
+GazeWorld	56.42	58.30	55.45	58.50	67.16	44.89	60.83	64.01	61.33
Δ	+0.33	+1.15	+0.42	+1.04	+0.31	+1.81	+1.06	+0.77	+0.29
MedCLIP	56.63	57.40	55.72	58.09	62.17	40.07	56.17	56.89	55.44
+GazeWorld	58.13	59.42	56.85	62.84	70.18	47.31	64.29	66.59	63.26
Δ	+1.50	+2.02	+1.13	+4.75	+8.01	+7.24	+8.12	+9.70	+7.82

4.5 Ablation Studies

Gaze ordering and objectives. Table 4 shows that chronological gaze order is critical: replacing expert scanpaths with raster-scan or random order substantially degrades zero-shot AUROC across all datasets, indicating that the gain is not merely due to ordered patch exposure. MedCLIP initialization performs best, suggesting that gaze-ordered prediction benefits from a semantically aligned medical visual backbone. Finally, AR-only already gives strong performance, while adding spatial completion further improves results; SC-only is weaker, suggesting that predicting unvisited anatomy without the autoregressive fixation context provides less effective supervision, and that completion is most beneficial when conditioned on chronological expert fixation dynamics.

Backbone initialization. Table 5 further evaluates whether GazeWorld can improve different medical visual backbones. Across MGCA, EGMA, and MedCLIP initializations, adding GazeWorld consistently improves zero-shot performance on the external benchmarks, showing that the proposed gaze-ordered world-model pretraining is not tied to a single backbone. These results suggest that GazeWorld can generally refine medical visual encoders with expert reading dynamics.

5 Conclusion

We introduced GazeWorld, a gaze-ordered world-model refinement objective for medical image representation learning. By predicting the next expert-fixated representation and completing unvisited anatomy in semantic space, GazeWorld injects radiologist reading dynamics into pretrained medical visual encoders. Experiments on diagnostic transfer, scanpath probing, and backbone initialization show that this objective improves task performance and better encodes expert visual-search struc-

ture, suggesting that modeling how radiologists gather evidence can complement existing medical pretraining paradigms.

Limitations . This study is limited to chest radiographs and one eye-tracking corpus. Future work should evaluate larger multi-reader gaze datasets, broader imaging modalities, and formal clinician-centered localization studies.

References

- Jeremy Irvin, Pranav Rajpurkar, Michael Ko, Yifan Yu, Silvana Ciurea-Ilcus, Chris Chute, Henrik Marklund, Behzad Haghgoo, Robyn Ball, Katie Shpanskaya, et al. Chexpert: A large chest radiograph dataset with uncertainty labels and expert comparison. In *Proceedings of the AAAI conference on artificial intelligence*, volume 33, pages 590–597, 2019.
- Alistair EW Johnson, Tom J Pollard, Seth J Berkowitz, Nathaniel R Greenbaum, Matthew P Lungren, Chih-ying Deng, Roger G Mark, and Steven Horng. Mimic-cxr, a de-identified publicly available database of chest radiographs with free-text reports. *Scientific data*, 6(1):317, 2019.
- Pranav Rajpurkar, Jeremy Irvin, Kaylie Zhu, Brandon Yang, Hershel Mehta, Tony Duan, Daisy Ding, Aarti Bagul, Curtis Langlotz, Katie Shpanskaya, et al. Chexnet: Radiologist-level pneumonia detection on chest x-rays with deep learning. *arXiv preprint arXiv:1711.05225*, 2017.
- Shekoofeh Azizi, Basil Mustafa, Fiona Ryan, Zachary Beaver, Jan Freyberg, Jonathan Deaton, Aaron Loh, Alan Karthikesalingam, Simon Kornblith, Ting Chen, et al. Big self-supervised models advance medical image classification. In *Proceedings of the IEEE/CVF international conference on computer vision*, pages 3478–3488, 2021.
- Hari Sowrirajan, Jingbo Yang, Andrew Y Ng, and Pranav Rajpurkar. Moco pretraining improves representation and transferability of chest x-ray models. In *Medical Imaging with Deep Learning*, pages 728–744. PMLR, 2021.
- Zhihong Chen, Maya Varma, Jean-Benoit Delbrouck, Magdalini Paschali, Louis Blankemeier, Dave Van Veen, Jeya Maria Jose Valanarasu, Alaa Youssef, Joseph Paul Cohen, Eduardo Pontes Reis, et al. Chexagent: Towards a foundation model for chest x-ray interpretation. In *AAAI 2024 Spring Symposium on Clinical Foundation Models*, 2024.
- Yukun Zhou, Mark A Chia, Siegfried K Wagner, Murat S Ayhan, Dominic J Williamson, Robbert R Struyven, Timing Liu, Moucheng Xu, Mateo G Lozano, Peter Woodward-Court, et al. A foundation model for generalizable disease detection from retinal images. *Nature*, 622(7981):156–163, 2023.
- Junjie Shentu and Noura Al Moubayed. Cxr-irgen: An integrated vision and language model for the generation of clinically accurate chest x-ray image-report pairs. In *Proceedings of the IEEE/CVF winter conference on applications of computer vision*, pages 5212–5221, 2024.
- Sheng Wang, Xi Ouyang, Tianming Liu, Qian Wang, and Dinggang Shen. Follow my eye: Using gaze to supervise computer-aided diagnosis. *IEEE Transactions on Medical Imaging*, 41(7):1688–1698, 2022a.
- Chong Ma, Hanqi Jiang, Wenting Chen, Yiwei Li, Zihao Wu, Xiaowei Yu, Zhengliang Liu, Lei Guo, Dajiang Zhu, Tuo Zhang, et al. Eye-gaze guided multi-modal alignment for medical representation learning. *Advances in Neural Information Processing Systems*, 37:6126–6153, 2024.
- Sheng Wang, Zihao Zhao, Zhenrong Shen, Bin Wang, Qian Wang, and Dinggang Shen. Improving self-supervised medical image pre-training by early alignment with human eye gaze information. *IEEE Transactions on Medical Imaging*, 44(10):4063–4072, 2025.
- Trong Thang Pham, Tien-Phat Nguyen, Yuki Ikebe, Akash Awasthi, Zhigang Deng, Carol C Wu, Hien Nguyen, and Ngan Le. Gazesearch: radiology findings search benchmark. In *2025 IEEE/CVF Winter Conference on Applications of Computer Vision (WACV)*, pages 96–106. IEEE, 2025.
- Dmitry Lvov and Ilya Pershin. From human attention to diagnosis: Semantic patch-level integration of vision-language models in medical imaging. In *The Thirty-ninth Annual Conference on Neural Information Processing Systems*, 2025.

- Yann LeCun et al. A path towards autonomous machine intelligence version 0.9. 2, 2022-06-27. *Open Review*, 62(1):1–62, 2022.
- Mahmoud Assran, Quentin Duval, Ishan Misra, Piotr Bojanowski, Pascal Vincent, Michael Rabbat, Yann LeCun, and Nicolas Ballas. Self-supervised learning from images with a joint-embedding predictive architecture. In *Proceedings of the IEEE/CVF conference on computer vision and pattern recognition*, pages 15619–15629, 2023.
- Errol Colak, Felipe C Kitamura, Stephen B Hobbs, Carol C Wu, Matthew P Lungren, Luciano M Prevedello, Jayashree Kalpathy-Cramer, Robyn L Ball, George Shih, Anouk Stein, et al. The rsna pulmonary embolism ct dataset. *Radiology: Artificial Intelligence*, 3(2):e200254, 2021.
- Andrew Zawacki, Carol Wu, George Shih, Julia Elliott, Mikhail Fomitchev, Mohannad Husain, Paras Lakhani, Phil Culliton, and Shunxing Bao. Siim-acr pneumothorax segmentation. Kaggle, 2019. Available at: <https://www.kaggle.com/competitions/siim-acr-pneumothorax-segmentation>.
- Khaled Saab, Sarah M Hooper, Nimit S Sohoni, Jupinder Parmar, Brian Pogatchnik, Sen Wu, Jared A Dunmmon, Hongyang R Zhang, Daniel Rubin, and Christopher Ré. Observational supervision for medical image classification using gaze data. In *International conference on medical image computing and computer-assisted Intervention*, pages 603–614. Springer, 2021.
- Joseph N Stember, Haydar Celik, E Krupinski, Peter D Chang, Simukayi Mutasa, Bradford J Wood, A Lignelli, Gul Moonis, Lawrence H Schwartz, Sachin Jambawalikar, et al. Eye tracking for deep learning segmentation using convolutional neural networks. *Journal of digital imaging*, 32(4): 597–604, 2019.
- Chihcheng Hsieh, André Luís, José Neves, Isabel Blanco Nobre, Sandra Costa Sousa, Chun Ouyang, Joaquim Jorge, and Catarina Moreira. Eyexnet: Enhancing abnormality detection and diagnosis via eye-tracking and x-ray fusion. *Machine Learning and Knowledge Extraction*, 6(2):1055–1071, 2024.
- Yogesh Kumar and Pekka Marttinen. Improving medical multi-modal contrastive learning with expert annotations. In *European Conference on Computer Vision*, pages 468–486. Springer, 2024.
- Sounak Mondal, Zhibo Yang, Seoyoung Ahn, Dimitris Samaras, Gregory Zelinsky, and Minh Hoai. Gazeformer: Scalable, effective and fast prediction of goal-directed human attention. In *Proceedings of the IEEE/CVF conference on computer vision and pattern recognition*, pages 1441–1450, 2023.
- Zhibo Yang, Sounak Mondal, Seoyoung Ahn, Ruoyu Xue, Gregory Zelinsky, Minh Hoai, and Dimitris Samaras. Unifying top-down and bottom-up scanpath prediction using transformers. In *Proceedings of the IEEE/CVF Conference on Computer Vision and Pattern Recognition*, pages 1683–1693, 2024.
- Akash Awasthi, Anh Mai Vu, Ngan Le, Zhigang Deng, Supratik Maulik, Rishi Agrawal, Carol C Wu, and Hien Van Nguyen. Modeling radiologists’ cognitive processes using a digital gaze twin to enhance radiology training. *Scientific reports*, 15(1):13685, 2025.
- Adrien Bardes, Quentin Garrido, Jean Ponce, Xinlei Chen, Michael Rabbat, Yann LeCun, Mido Assran, and Nicolas Ballas. V-jepa: Latent video prediction for visual representation learning. 2023.
- Mark Chen, Alec Radford, Rewon Child, Jeffrey Wu, Heewoo Jun, David Luan, and Ilya Sutskever. Generative pretraining from pixels. In *International conference on machine learning*, pages 1691–1703. PMLR, 2020.
- Alaaeldin El-Nouby, Michal Klein, Shuangfei Zhai, Miguel Angel Bautista, Alexander Toshev, Vaishaal Shankar, Joshua M Susskind, and Armand Joulin. Scalable pre-training of large autoregressive image models. *arXiv preprint arXiv:2401.08541*, 2024.
- Yang Yue, Yulin Wang, Chenxin Tao, Pan Liu, Shiji Song, and Gao Huang. Chexworld: Exploring image world modeling for radiograph representation learning. In *Proceedings of the Computer Vision and Pattern Recognition Conference*, pages 20778–20788, 2025.

- Ashwath Radhachandran, Vedrana Ivezic, Shreeram Athreya, Ronit Anilkumar, Corey W Arnold, and William Speier. Us-jepa: A joint embedding predictive architecture for medical ultrasound. *arXiv preprint arXiv:2602.19322*, 2026.
- Junfei Xiao, Yutong Bai, Alan Yuille, and Zongwei Zhou. Delving into masked autoencoders for multi-label thorax disease classification. In *Proceedings of the IEEE/CVF winter conference on applications of computer vision*, pages 3588–3600, 2023.
- Shih-Cheng Huang, Liyue Shen, Matthew P Lungren, and Serena Yeung. Gloria: A multimodal global-local representation learning framework for label-efficient medical image recognition. In *Proceedings of the IEEE/CVF international conference on computer vision*, pages 3942–3951, 2021.
- Zifeng Wang, Zhenbang Wu, Dinesh Agarwal, and Jimeng Sun. Medclip: Contrastive learning from unpaired medical images and text. In *Proceedings of the 2022 Conference on Empirical Methods in Natural Language Processing*, pages 3876–3887, 2022b.
- Shruthi Bannur, Stephanie Hyland, Qianchu Liu, Fernando Perez-Garcia, Maximilian Ilse, Daniel C Castro, Benedikt Boecking, Harshita Sharma, Kenza Bouzid, Anja Thieme, et al. Learning to exploit temporal structure for biomedical vision-language processing. In *Proceedings of the IEEE/CVF conference on computer vision and pattern recognition*, pages 15016–15027, 2023.
- Fuying Wang, Yuyin Zhou, Shujun Wang, Varut Vardhanabhuti, and Lequan Yu. Multi-granularity cross-modal alignment for generalized medical visual representation learning. *Advances in neural information processing systems*, 35:33536–33549, 2022c.
- Chaoyi Wu, Xiaoman Zhang, Ya Zhang, Yanfeng Wang, and Weidi Xie. Medklip: Medical knowledge enhanced language-image pre-training for x-ray diagnosis. In *Proceedings of the IEEE/CVF international conference on computer vision*, pages 21372–21383, 2023.
- Pujin Cheng, Li Lin, Junyan Lyu, Yijin Huang, Wenhan Luo, and Xiaoying Tang. Prior: Prototype representation joint learning from medical images and reports. In *Proceedings of the IEEE/CVF international conference on computer vision*, pages 21361–21371, 2023.
- Jean-Bastien Grill, Florian Strub, Florent Alché, Corentin Tallec, Pierre Richemond, Elena Buchatskaya, Carl Doersch, Bernardo Avila Pires, Zhaohan Guo, Mohammad Gheshlaghi Azar, et al. Bootstrap your own latent—a new approach to self-supervised learning. *Advances in neural information processing systems*, 33:21271–21284, 2020.
- Chihcheng Hsieh, Chun Ouyang, Jacinto C Nascimento, Joao Pereira, Joaquim Jorge, and Catarina Moreira. Mimic-eye: Integrating mimic datasets with reflax and eye gaze for multimodal deep learning applications. *PhysioNet (version 1.0. 0)*, 2023.
- Ze Liu, Yutong Lin, Yue Cao, Han Hu, Yixuan Wei, Zheng Zhang, Stephen Lin, and Baining Guo. Swin transformer: Hierarchical vision transformer using shifted windows. In *Proceedings of the IEEE/CVF international conference on computer vision*, pages 10012–10022, 2021.
- Ilya Loshchilov and Frank Hutter. Decoupled weight decay regularization. *arXiv preprint arXiv:1711.05101*, 2017.
- Ramprasaath R Selvaraju, Michael Cogswell, Abhishek Das, Ramakrishna Vedantam, Devi Parikh, and Dhruv Batra. Grad-cam: Visual explanations from deep networks via gradient-based localization. In *Proceedings of the IEEE international conference on computer vision*, pages 618–626, 2017.
- Alec Radford, Jong Wook Kim, Chris Hallacy, Aditya Ramesh, Gabriel Goh, Sandhini Agarwal, Girish Sastry, Amanda Askell, Pamela Mishkin, Jack Clark, et al. Learning transferable visual models from natural language supervision. In *International conference on machine learning*, pages 8748–8763. PmlR, 2021.
- Filipe Cristino, Sebastiaan Mathôt, Jan Theeuwes, and Iain D Gilchrist. Scanmatch: A novel method for comparing fixation sequences. *Behavior research methods*, 42(3):692–700, 2010.

- Tom Foulsham and Geoffrey Underwood. What can saliency models predict about eye movements? spatial and sequential aspects of fixations during encoding and recognition. *Journal of vision*, 8(2): 6–6, 2008.
- Wei Wang, Cheng Chen, Yizhou Wang, Tingting Jiang, Fang Fang, and Yuan Yao. Simulating human saccadic scanpaths on natural images. In *CVPR 2011*, pages 441–448. IEEE, 2011.
- Halszka Jarodzka, Kenneth Holmqvist, and Marcus Nyström. A vector-based, multidimensional scanpath similarity measure. In *Proceedings of the 2010 symposium on eye-tracking research & applications*, pages 211–218, 2010.
- Laurens Van der Maaten and Geoffrey Hinton. Visualizing data using t-sne. *Journal of machine learning research*, 9(11), 2008.

A Baseline Protocol Details

A.1 Dataset Details

MIMIC-EYE. MIMIC-EYE [Hsieh et al., 2023] is an eye-tracking extension of the MIMIC-CXR database [Johnson et al., 2019]. It records radiologist fixation sequences from 3,032 frontal chest radiographs during routine clinical reading sessions using a Tobii Pro Nano eye tracker (sampling rate 60 Hz). Each record contains a temporally ordered sequence of fixation coordinates (x_t, y_t) with associated dwell durations. We split the data into 2,729 / 151 / 152 train/val/test following the official partition. Per-image fixation sequences average 47 fixation points; after de-duplication to unique patch indices, the resulting sequence is used as the causal order for world-model pretraining.

GazeSearch (ChestSearch protocol). GazeSearch [Pham et al., 2025] provides task-directed eye-tracking data: radiologists search for specific pathologies (13 finding categories) on chest radiographs. The ChestSearch split contains 3,870 training and 488 test samples, each consisting of a radiograph, a target pathology label, and a ground-truth fixation sequence (up to 7 fixations).

CheXpert. CheXpert [Irvin et al., 2019] is a large-scale chest radiograph dataset containing 224,316 images from 65,240 patients at Stanford Hospital, labeled for 14 observations via an automated NLP labeler applied to radiology reports. We evaluate on 5 competition pathologies (Atelectasis, Cardiomegaly, Consolidation, Edema, Pleural Effusion) under 1%, 10%, and 100% label fractions. For zero-shot evaluation, we follow the CheXpert 5×200 protocol [Ma et al., 2024]: 200 images per class, 5 pathologies.

RSNA Pneumonia. The RSNA [Colak et al., 2021] Pneumonia Detection Challenge dataset provides 26,684 frontal chest radiographs with bounding-box annotations for pneumonia opacities, curated from the NIH ChestX-ray14 collection. We use the binary pneumonia/normal classification task under 1%, 10%, and 100% label fractions.

SIIM-ACR Pneumothorax. The SIIM-ACR Pneumothorax Segmentation dataset [Zawacki et al., 2019] contains 12,047 chest radiographs with pixel-level pneumothorax masks. We convert it to a binary classification task (pneumothorax-present vs. normal) and evaluate under 1%, 10%, and 100% label fractions.

A.2 Baseline Comparison Protocol

Table 6 summarizes the backbone architecture, pretraining data, and result provenance for every baseline in the main comparison tables.

Classification baselines. All classification numbers for BioViL, MedKLIP, MGCA, GLoRIA, PRIOR, MedCLIP, and EGMA in Tables 1 and 2 are taken from EGMA [Ma et al., 2024], which re-evaluated every method under a single downstream protocol. The EGMA protocol fixes the following variables across all methods: (i) train/val/test splits, (ii) downstream head, (iii) optimizer and schedule, (iv) number of fine-tuning epochs, and early-stopping criterion, and (v) metric computation.

The protocol does not harmonize backbone architecture: BioViL, MedKLIP, MGCA, GLORIA, and PRIOR use ResNet-50, while MedCLIP, EGMA, and our method use Swin-Tiny. Therefore, comparisons against ResNet-50-based baselines include both objective and backbone differences.

Controlled comparison (Ours vs. EGMA). The cleanest comparison in our evaluation is Ours vs. EGMA. Both methods share the same Swin backbone, the same MedCLIP initialization weights, the same MIMIC-EYE fixation data, and the same downstream evaluation protocol. The only variable is the pretraining objective applied on top of MedCLIP: EGMA uses gaze-guided contrastive alignment, while we use the GazeWorld world-model objective. Performance differences between these two rows in Tables 1–2 therefore isolate the contribution of the pretraining objective with minimal confounds.

Scanpath baselines. Scanpath prediction baselines in Table 3 are evaluated under the ChestSearch protocol. We use the original paper results for LogitGaze-Med and evaluate GazeFormer, HAT, GazeSearch, and LogitGaze using their official implementations under the same protocol. Our scanpath decoder uses the same evaluation protocol (7 fixations, the same test split of 488 samples, and the same metrics). For the scanpath probe, the decoder architecture and training procedure are held fixed across backbone variants.

Resolution and backbone notes. For classification (Tables 1 and 2), all methods use 224×224 input resolution. For scanpath prediction (Table 3), our decoder and the primary baselines operate at 448×448 ; GazeFormer and HAT use 224×224 but are included for completeness as earlier methods.

B Implementation Details

Backbone. We use the MedCLIP Swin image encoder [Liu et al., 2021] as the online visual backbone. The encoder has 4 stages, embedding dimension $C = 96$, window size 7, patch size 4, and output dimension $d = 768$. Unless otherwise specified, chest radiographs are resized to 224×224 for representation learning, yielding patch-level semantic tokens

$$\mathbf{Z} = \phi(\mathbf{X}) = \{\mathbf{z}_p\}_{p=1}^N, \quad \mathbf{z}_p \in \mathbb{R}^{768}. \quad (13)$$

During world-model pretraining, the online visual encoder is updated jointly with the gaze-conditioned modules. A separate momentum target encoder provides stop-gradient representation-space targets.

Fixation preprocessing. Each eye-tracking record provides a temporally ordered sequence of fixation coordinates with associated dwell durations. Fixation coordinates are normalized to the image frame and mapped to the nearest patch index. Repeated visits to the same patch are merged while preserving the first-visit order, yielding a fixation-ordered sequence of unique visited patches $\mathcal{S} = (s_1, \dots, s_L)$. This sequence defines the causal prediction order used by the autoregressive world model.

Fixation embedder. For each visited patch s_i , the fixation embedder combines the visual patch token \mathbf{z}_{s_i} with three fixation-specific signals: a two-dimensional spatial embedding of the patch location, a learned temporal-rank embedding for the fixation order i , and a projected dwell-duration feature. The resulting fixation token is used as input to the causal predictor.

Autoregressive predictor. The autoregressive predictor is an 8-layer causal Transformer with 12 attention heads, head dimension 64, hidden dimension $d = 768$, and a lower-triangular causal attention mask. It receives previously fixated tokens and predicts the semantic representation of the next fixated patch. The prediction head is a two-layer MLP with GELU activation.

Momentum target encoder. To provide stable representation-space targets, we maintain a target encoder $\bar{\phi}$ as an exponential-moving-average copy of the online visual encoder ϕ . The target encoder is evaluated under no-gradient computation and is not directly updated by back-propagation. After each optimizer step, its parameters are updated as

$$\bar{\theta}_\phi \leftarrow \tau \bar{\theta}_\phi + (1 - \tau) \theta_\phi, \quad (14)$$

where θ_ϕ and $\bar{\theta}_\phi$ denote the parameters of the online and target visual encoders, respectively. The EMA momentum follows a cosine schedule from 0.998 to 1.0.

Spatial-completion decoder. The spatial-completion branch is a lightweight 2-layer cross-attention decoder with hidden dimension $d = 768$. Let $\mathcal{U} = \{1, \dots, N\} \setminus \{s_1, \dots, s_L\}$ denote the set of unvisited patches. For each $p \in \mathcal{U}$, the decoder forms a query by adding a learnable mask token to the spatial embedding of patch p . The keys and values are the gaze-context tokens produced by the causal predictor. The decoder outputs one predicted representation $\hat{\mathbf{r}}_p$ for each unvisited patch, which is matched to the corresponding momentum-target representation $\bar{\mathbf{z}}_p$.

Pretraining objective. The world-model pretraining objective combines autoregressive next-fixation prediction and spatial completion:

$$\mathcal{L} = \mathcal{L}_{\text{AR}} + \lambda \mathcal{L}_{\text{SC}}. \quad (15)$$

In all main experiments, we set the spatial-completion weight to $\lambda = 1.0$. The autoregressive loss is

$$\mathcal{L}_{\text{AR}} = \frac{1}{L-1} \sum_{i=2}^L \text{SmoothL1}(\text{LN}(\hat{\mathbf{z}}_{s_i}), \text{sg}(\bar{\mathbf{z}}_{s_i})), \quad (16)$$

and the spatial-completion loss is

$$\mathcal{L}_{\text{SC}} = \frac{1}{|\mathcal{U}|} \sum_{p \in \mathcal{U}} \text{SmoothL1}(\text{LN}(\hat{\mathbf{r}}_p), \text{sg}(\text{LN}(\bar{\mathbf{z}}_p))). \quad (17)$$

Here, $\text{LN}(\cdot)$ denotes layer normalization and $\text{sg}(\cdot)$ denotes stop-gradient.

Optimization. We train the world model on MIMIC-EYE using AdamW [Loshchilov and Hutter, 2017] with learning rate 3×10^{-4} , weight decay 0.04, batch size 32, automatic mixed precision, and 15 training epochs. The online MedCLIP-Swin encoder, fixation embedder, causal predictor, autoregressive prediction head, and spatial-completion decoder are optimized jointly. The target encoder receives no gradients and is updated only through EMA.

Scanpath decoder. GazeSearch train split: 3,870 samples. AdamW, learning rate 5×10^{-4} , weight decay 0.01, cosine annealing ($\eta_{\min} = 10^{-6}$, $T_{\max} = 30$), batch size 16, 30 epochs. Best checkpoint selected by validation mean Euclidean distance; evaluation on 488 test samples.

Linear probing. We evaluate frozen pretrained representations on CheXpert (14-class), RSNA Pneumonia, and SIIM-ACR Pneumothorax at 1%, 10%, and 100% label fractions. For each image we extract a 1536-d feature by concatenating two halves: (i) the mean-pooled patch tokens of the online MedCLIP-Swin encoder ϕ , and (ii) the d -dimensional output of a learnable readout token prepended to a deterministic raster-scan surrogate fixation sequence over the N patches and processed by the (frozen) causal predictor, followed by a learned linear projection back to d . No gaze annotations are used at probing time. Features are standardised per dimension (zero mean, unit variance) and fed to an ℓ_2 -regularised logistic-regression classifier (LBFGS, $C=1$, 2000 iterations); training fractions are sampled with a fixed seed. We report 14-class macro AUROC on CheXpert and binary AUROC on RSNA / SIIM-ACR. The backbone and predictor receive no gradient at probing time.

C Attention Heatmap Protocol

The attention heatmaps in Figure 2 are generated using Grad-CAM [Selvaraju et al., 2017], following the same protocol as EGMA [Ma et al., 2024] to ensure visual comparability. For each image–pathology pair: (i) the frozen backbone used for downstream evaluation processes the image at 224×224 ; (ii) we compute the gradient of the target pathology logit with respect to the feature maps of the final convolutional stage (Swin-Tiny stage 4 for our method and EGMA; the corresponding final block for ResNet-50-based methods); (iii) feature maps are globally average-pooled along the channel dimension using the gradient magnitudes as weights; (iv) the resulting spatial map is ReLU-activated, upsampled to input resolution via bilinear interpolation, and min–max normalized to $[0, 1]$. All methods use the same Grad-CAM implementation and the same set of test images. Grad-CAM visualizations are qualitative: they indicate which spatial regions most influence a particular logit but do not provide localization guarantees.

Table 6: Baseline comparison protocol. “Reported” indicates numbers taken from the cited paper under its original or unified evaluation protocol; “Rerun” indicates our own execution. For our method, the input resolution follows the corresponding evaluation setting: 224 for classification and 448 for scanpath probing, to match the protocol used in each experiment.

Method	Backbone	Pretrain data	Resolution	Source
BioViL	ResNet	MIMIC-CXR	224	Rerun
MedKLIP	ResNet	MIMIC-CXR	224	Rerun
MGCA	ResNet	MIMIC-CXR	224	Rerun
GLoRIA	ResNet	CheXpert	224	Rerun
PRIOR	ResNet	MIMIC-CXR	224	Rerun
MedCLIP	Swin	MIMIC-CXR	224	Rerun
CheXWorld	ViT	MIMIC-CXR	224	Rerun
EGMA	Swin	MIMIC-CXR + EYE	224	Rerun
GazeFormer	ViT	ImageNet + COCO	224	Rerun
HAT	ResNet	ImageNet	224	Reported (GazeSearch)
GazeSearch	ResNet	ImageNet	448	Rerun
LogitGaze-Med	ResNet / CheX	MIMIC-CXR + EYE	448	Reported (LogitGaze)
Ours	Swin	MIMIC-CXR + EYE	224/448	Rerun

D Scanpath Decoder Architecture

The input is resized to 448×448 , yielding a 14×14 patch grid ($N = 196$) for finer spatial resolution. Patch features are projected from $d = 768$ to $d_s = 512$ via a linear layer. The decoder receives three inputs: the projected patch features, a learned task embedding $\mathbf{t} \in \mathbb{R}^{d_s}$ indicating which pathology to search for ($t \in \{0, \dots, 12\}$), and the initial fixation coordinate $\mathbf{x}_0 = (0.5, 0.5)$, projected to d_s dimensions.

At each step, the current fixation token queries the full set of patch features via cross-attention. A causal Transformer (6 layers, 8 heads, dimension $d_s = 512$) processes the growing fixation sequence with temporal positional encoding. Three output heads operate on each hidden state \mathbf{h}_t : (i) a spatial head, implemented as a 196-way softmax over the patch grid; (ii) a duration head that regresses fixation dwell time; and (iii) a termination head. Following the GazeSearch evaluation protocol, the decoder emits 7 fixations at inference time. The scanpath loss is

$$\mathcal{L}_{\text{scan}} = \mathcal{L}_{\text{spatial}}(\text{CE}, 196) + 0.1 \cdot \mathcal{L}_{\text{dur}}(\ell_1) + 0.1 \cdot \mathcal{L}_{\text{term}}(\text{BCE}). \quad (18)$$

Only the decoder parameters are trained during scanpath probing; the backbone remains frozen in this probing stage. The scanpath loss is never back-propagated into the backbone.

E Representation Visualization

Figure 4 provides a qualitative visualization of the learned representation space on the CheXpert 5×200 dataset. CLIP features show considerable mixing across pathology categories, while EGMA produces partial separation with remaining inter-class overlap. Our method shows clearer pathology-level grouping, with more compact clusters for categories such as Cardiomegaly and Pleural Effusion. Since t-SNE [Van der Maaten and Hinton, 2008] is a qualitative projection and can be sensitive to hyperparameters, we use this visualization only as supporting evidence; the quantitative transfer results in Tables 1 and 2 provide the primary evaluation of representation quality.

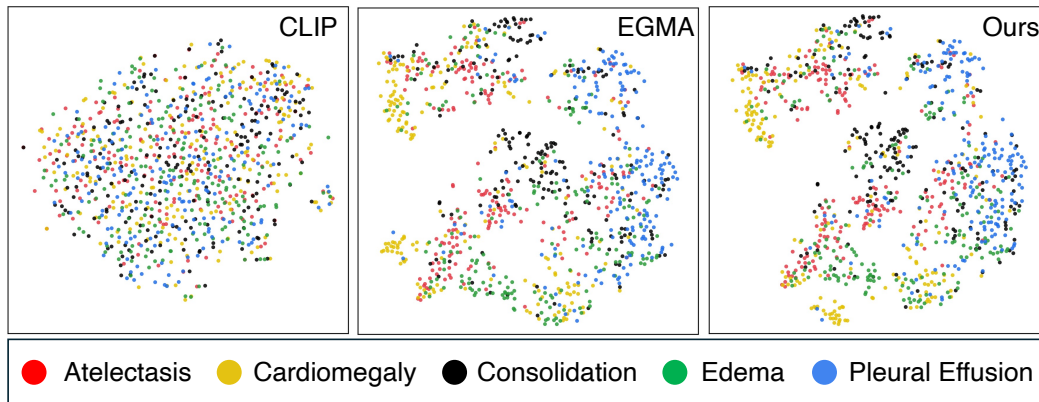


Figure 4: t-SNE visualization of learned representations on the CheXpert 5×200 dataset. Each point represents a chest radiograph and is color-coded by its ground-truth pathology label.